

Experimental Multi-Frequency Data for a Globally Convergent Numerical Method for an Inverse Scattering Problem

Dinh-Liem Nguyen* Michael V. Klibanov* Loc H. Nguyen*
 Aleksandr E. Kolesov*[†] Michael A. Fiddy[‡] Hui Liu*

Abstract

This paper is concerned with the inverse problem of determining the dielectric constant and geometric information of three-dimensional scattering objects from experimental frequency-domain backscatter data corresponding to a single incident wave. These multi-frequency data are collected using a microwave scattering facility at the University of North Carolina at Charlotte. The challenges for the inverse problem under consideration are not only from its nonlinearity and high ill-posedness but also from the fact that the experimental data have a huge misfit with data obtained in simulations. We present in this paper how the raw data can be preprocessed and successfully inverted using a globally convergent numerical method. More precisely, we are able to reconstruct the dielectric constant of the scattering medium with a reasonable accuracy as well as its geometric information such as location and size without using any detailed *a priori* knowledge of physical and geometrical properties of the medium. We note that the latter feature is the essential difference between our globally convergent approach and nonlinear optimization approaches, which are often referred to as locally convergent methods for inverse problems.

Key words. experimental multi-frequency data, backscatter data, inverse scattering, globally convergent methods, coefficient identification, microwave imaging

AMS subject classifications. 35R30, 35L05, 78A46

1 Introduction

We consider the inverse scattering problem of reconstruction of physical and geometrical properties of three-dimensional objects from experimental multi-frequency data without using

*Department of Mathematics and Statistics, University of North Carolina at Charlotte, Charlotte, NC 28223, USA; (dnguye70@uncc.edu, mklibanv@uncc.edu, lnguye50@uncc.edu, akolesov@uncc.edu, hliu34@uncc.edu)

[†]Institute of Mathematics and Information Science, North-Eastern Federal University, Yakutsk, Russia; (ae.kolesov@s-vfu.ru)

[‡]Optoelectronics Center, University of North Carolina at Charlotte, Charlotte, NC 28223, USA; (mafiddy@uncc.edu)

any detailed a priori knowledge of the targets. These targets are placed in air, and the measured data are the backscatter corresponding to a single incident wave. Our study is mainly motivated by potential applications in detection and identification of explosives such as, e.g., anti-personnel mines and improvised explosive devices (IEDs), see [26, 30]. We note that IEDs are also often buried under the ground for which one needs to study the corresponding inverse problem of determining buried objects. This topic is subject to a future publication, although such a study was performed by our group in an earlier publication using a different globally convergent inverse method [28]. At the same time, both IEDs and mines can often be located in air and our current study models this case. The idea here is to determine the dielectric constants of targets. The knowledge of dielectric constants might serve in the future classification algorithms as a piece of information, which would be an additional one to those commonly currently used in the radar community. Indeed, this community relies now only on the intensity of radar images, see, e.g., [20]. It is well known that the question of a reliable differentiation between explosives and clutter is not yet addressed satisfactory in the radar community. So, estimates of dielectric constants and of shapes of targets combined with the image intensity and other parameters might lead in the future to such classification algorithms, which would address this question better. The second potential application of our study is in nondestructive testing and materials characterization.

The problem under consideration is also called the inverse medium problem or the coefficient inverse problem, i.e., the problem of recovering of a coefficient of a partial differential equation from boundary measurements. There is a large body of literature on imaging methods for reconstructing geometric information about targets, such as their shapes, sizes and locations. We refer to, e.g., [8, 24, 25] and references therein for well-known imaging techniques in inverse scattering such as level set methods, sampling methods, migration methods and shape optimization methods. However, for detecting or identifying, for instance, IEDs, it would be certainly the physical properties of the target (in our model, the dielectric constant), playing a more important role [30]. Furthermore, determining the spatially distributed dielectric constants, which is of our main interest, is known to be a more difficult task since this is a coefficient inverse problem.

Among the inversion methods developed for solving the coefficient inverse problems, the two probably most well known approaches are nonlinear approximation schemes and weak scattering approximation methods such as Born approximation and physical optics, see, e.g., [13]. The weak scattering approximation is not applicable to the inverse problem under consideration, where the scattering objects can be strong scatterers. Regarding the nonlinear optimization approaches or also known as iterative solution methods, we refer to [1, 7, 9, 12, 15] and references therein. It is well-known that the convergence for this class of methods typically requires a good a priori initial approximation of the exact solution, that is, the starting point of iterations should be chosen to be sufficiently close to the solution. Hence, we call such methods locally convergent. We note that in our desired applications such a priori knowledge is not always available.

This limitation of nonlinear optimization approaches is avoided in the so-called approximately globally convergent method (globally convergent method, for short, or GCM), which has been recently introduced by the second author and a collaborator, see [2]. The GCM,

which does not use optimization schemes, aims to provide a good approximation to the solution of the coefficient inverse problem without using any detailed a priori knowledge of the solution. More precisely, the concept “approximately globally convergence” can be understood in the language of functional analysis as follows: under some reasonable approximate mathematical assumption the method provides at least one point in a sufficiently small neighborhood of the exact coefficient without a priori knowledge of any point in this neighborhood. The accuracy of the approximation or the distance between those points and the exact solution depends on the error in the data and some parameters of the discretization. We point out that the fact of the proximity of that point to the correct coefficient, which was achieved without any a priori knowledge of that small neighborhood, is the main advantage of our globally convergent method over locally convergent ones. Indeed, as soon as one knows a point in a sufficiently small neighborhood of the true solution, one can refine it via a locally convergent method, see, e.g., [2, Chapter 4]. The latter, however, is outside of the scope of the current publication. We refer to [2, Theorem 2.9.4] and [3] for more details about the definition of the global convergence as well as a rigorous mathematical analysis of the global convergence of the method relying on some approximate mathematical framework.

The performance of the GCM for experimental data has been investigated in [2, 18, 20, 27, 28]. We remark that in most of established results for the GCM the model of hyperbolic wave type equations is considered and the time-domain problem is converted into the pseudo-frequency domain problem via the Laplace transform. Consequently, all past experimental data studies for the method addressed the time-domain data. We note that since the Laplace transform used in the method has an exponentially decaying kernel, one likely loses some information in taking this transform of the (far field) measured data. To improve the performance of the GCM and to extend its direct application to multi-frequency data, which is common in applications to materials characterization [10], a Fourier transform version of the GCM has been recently developed in [19]. By Fourier transform version we mean an extension of the GCM for the inverse scattering problem for the Helmholtz equation. In the paper [19] numerical examples for simulated data are also presented.

As a continuation of the work of [19], the goal of this paper is to analyze the performance of the refined GCM for multi-frequency experimental data that were collected using a microwave scattering facility at the University of North Carolina at Charlotte. The descriptions above already state the new features of the present paper. To summarize it again, the globally convergent approach together with its advantages makes this work different from previously known locally convergent methods. Compared to the previous works of our group on experimental data, this one is the first where we study the experimental multi-frequency data for the refined GCM of [19]. The data preprocessing procedure for these multi-frequency data, discussed in the next paragraph, is substantially different from that of the time domain data in [27]. Furthermore, we remark that our measured data are stable only on a small interval of frequencies surrounding the central frequency of 3.1 GHz, see section 4.2.2. Therefore, transforming these data into time domain by the inverse Fourier transform may lead to a large inaccuracy in the time-dependent data obtained. That means that time domain inversion techniques including the previous versions of GCM [2] are not a good candidate for the inverse problem under consideration.

It is worth to mention that there has been a considerable interest on testing inversion algorithms against experimental data, see, e.g., [4, 22]. The data in the latter papers, which are from the Institute Fresnel’s database, were collected in an anechoic chamber which would prevent the data from being corrupted by unwanted signals generated by reflections from various objects in the room. These data are actually very well matched to those in simulations as described in [14]. The inversion methods tested for these data are among the most popular approaches mentioned above for the coefficient inverse problems. However, keeping in mind our desired application to the detection and identification of IEDs, we did not arrange a special anechoic chamber. Our data has been collected in a more realistic condition of a regular room, that is, the room contains office furniture, computers, etc., see Figure 1. This leads to the fact that the measured data and the simulated data have a huge misfit, see Figure 2, which is a true challenge for any inversion method. We note that conventional data denoising techniques do not help with the measured data because of its richer structure. We hence present a *heuristic* data preprocessing procedure, which aims to make the raw data look somewhat similar to the corresponding simulated data. The preprocessed data are then used as the input for the GCM. Our test results show that the GCM can reconstruct the dielectric constant of the scattering objects with a good accuracy as well as its geometric information such as location. In doing so, we do not use any detailed a priori knowledge on physical and geometrical properties of the targets.

The paper is organized as follows. In section 2, we state the forward and inverse scattering problems. Section 3 is devoted to a short description of the globally convergent method. We describe in section 4 the data collection and the steps of data preprocessing. Section 5 contains a description of the numerical implementation of the method and a summary of reconstruction results.

2 The forward and inverse scattering problem

In this section we formulate the forward and inverse problems for scattering of electromagnetic waves by a penetrable inhomogeneous medium in \mathbb{R}^3 in a certain range of the frequency ω . Below $\mathbf{x} = (x, y, z) \in \mathbb{R}^3$. We assume that the scattering medium, which occupies a bounded domain $D \subset \mathbb{R}^3$, is isotropic, non-magnetic and that it is characterized by the spatially distributed dielectric constant $\varepsilon_r(\mathbf{x})$, which is also called the relative permittivity. It is well known that, see for instance [5, Chapter 13], if $\varepsilon_r(\mathbf{x})$ varies slowly enough on the scales of the wavelength, then the scattering problem for Maxwell’s equations can be approximated by the scalar Helmholtz problem for a certain component of the electric field as follows

$$\Delta u + k^2 \varepsilon_r(\mathbf{x})u = 0, \quad \mathbf{x} \in \mathbb{R}^3, \quad (1)$$

$$u = e^{ikz} + u_{sc}, \quad (2)$$

$$\lim_{r \rightarrow \infty} r \left(\frac{\partial u_{sc}}{\partial r} - ik u_{sc} \right) = 0, \quad r = |\mathbf{x}|. \quad (3)$$

Here $k = \omega/c$ is the wavenumber with the speed of light c . The total field u is the sum of the scattered field u_{sc} and the incident field $u_{inc} = e^{ikz}$, propagating along the z -direction

toward the scattering medium. We note that the scattered field u_{sc} satisfies the Sommerfeld radiation condition (3), which guarantees that it is an outgoing wave.

We assume that $\varepsilon_r(\mathbf{x})$ is frequency-independent, real-valued, $\varepsilon_r \in C^1(\mathbb{R}^3)$ and that there exists a positive constant $c_u > 1$ such that

$$1 \leq \varepsilon_r(\mathbf{x}) \leq c_u, \quad \varepsilon_r(\mathbf{x}) = 1 \quad \text{for all } \mathbf{x} \in \mathbb{R}^3 \setminus \overline{D}. \quad (4)$$

The latter condition in (4) means that the medium outside D is homogeneous. It is well-known that the forward problem (1)–(3) of finding the total field u , given u_{inc} and ε_r , is uniquely solvable for $u \in C^2(\mathbb{R}^3)$, see [11, Chapter 8]. Our assumption of the frequency independence of ε_r is justified by the fact that in our inverse algorithm of [19] we actually work on a small interval of wavenumbers k . Our direct experimental measurements of the dielectric constants of targets have shown that they vary slowly with respect to k on small k -intervals.

We now formulate our inverse problem which is the main subject of the paper. To this end let us define $\Omega \subset \mathbb{R}^3$ as a convex bounded domain with its regular boundary $\partial\Omega$ such that $D \subset \Omega$, $\partial D \cap \partial\Omega = \emptyset$. Let \underline{k} and \overline{k} be positive constants such that $\underline{k} < \overline{k}$. Let $\Gamma \subset \partial\Omega$ be the part of the boundary $\partial\Omega$ which corresponds to the backscatter side of Ω . We consider the following inverse scattering problem or also the coefficient inverse problem:

Coefficient Inverse Problem. Assume that we are given a multi-frequency backscatter data $g(\mathbf{x}, k)$ defined by

$$g(\mathbf{x}, k) := u(\mathbf{x}, k), \quad \text{for } \mathbf{x} \in \Gamma, k \in [\underline{k}, \overline{k}], \quad (5)$$

where $u(\mathbf{x}, k)$ is the total field in the forward problem (1)–(3). Determine the relative permittivity $\varepsilon_r(\mathbf{x})$ for $\mathbf{x} \in \Omega$.

Remark 1 *The mathematical justification of the globally convergent method [19] has been done only for measurements on the entire boundary $\partial\Omega$. In our numerical implementation we would need to complement the backscatter data on the rest of the boundary $\partial\Omega$. We show how this is done in section 5.2.*

Since we consider only a single direction of the incident plane wave $u_{inc}(\mathbf{x}, k)$, then this is an inverse problem with single measurement data. Given such data, we emphasize that in our coefficient inverse problem we aim to reconstruct the coefficient $\varepsilon_r(\mathbf{x})$ using a numerical algorithm. The question whether $\varepsilon_r(\mathbf{x})$ can be uniquely determined from the data is outside of the scope of this paper. This is also one of the fundamental theoretical questions in the field of inverse problems.

The first uniqueness result for multidimensional coefficient inverse problems with single measurement data was established in [6], where the authors introduced a method based on Carleman estimates. This method has been extensively studied by a number of authors for uniqueness theorems in inverse problems with a finite number of measurements. We refer to [2, 17, 31] and references therein for surveys of this method and uniqueness results. However, the technique of [6] works only if a non-vanishing function $f(\mathbf{x})$ stands in the right hand side of (1). Hence, we always assume below that uniqueness result holds true.

We end up this section with the Lippmann-Schwinger equation formulation for the forward problem (1)–(3). Let the wavenumber k be fixed in (1)–(3). The Green’s function in free space for the forward problem is given by

$$\Phi_k(\mathbf{x}, \mathbf{y}) = \frac{\exp(ik|\mathbf{x} - \mathbf{y}|)}{4\pi|\mathbf{x} - \mathbf{y}|}, \quad \mathbf{x} \neq \mathbf{y}.$$

It is well-known that, see [11, Chapter 8], the forward problem (1)–(3) is equivalent to the Lippmann-Schwinger equation

$$u(\mathbf{x}) = e^{ikz} + k^2 \int_{\Omega} \Phi_k(\mathbf{x}, \mathbf{y})(\varepsilon_r(\mathbf{y}) - 1)u(\mathbf{y})d\mathbf{y}, \quad \mathbf{x} \in \mathbb{R}^3. \quad (6)$$

We observe from (6) that if we know the function $u(\mathbf{x})$ in Ω , then we can just extend it to $\mathbf{x} \in \mathbb{R}^3 \setminus \overline{\Omega}$ by the integration in (6). Hence, to solve (6), it is sufficient to find the function $u(\mathbf{x})$ only for points $\mathbf{x} \in \Omega$. This integral equation plays an important role for the convergence analysis of [19] as well as for the numerical algorithm of the globally convergent method, see section 3.3.

3 The globally convergent method

We describe in this section the globally convergent method together with its numerical algorithm. We essentially rely on the paper [19] where a theoretical study for this version of the method has been carried out for measurement data on the entire boundary $\partial\Omega$. Therefore, even though we are given only experimental backscatter data, we will assume that we have the complete data on $\partial\Omega$ for our description of the method.

3.1 Integro-differential equation formulation

The first crucial step for the construction of the GCM is to formulate the coefficient inverse problem as a nonlinear integro-differential equation. This is different from locally convergent methods with iterative optimization processes which typically rely on least-squares formulation. We describe in this section how to derive this integro-differential equation using the structure of the forward problem and a change of variables. To follow the theory of [19], we assume below that numbers \underline{k}, \bar{k} , which are given in (5), are sufficiently large and $k \in [\underline{k}, \bar{k}]$. It was shown in [19] that $u(\mathbf{x}, k) \neq 0$ for $\mathbf{x} \in \Omega$ as long as k is sufficiently large.

It has been shown in [19] that there exists a function $v(\mathbf{x}, k) \in C^2(\overline{\Omega})$ such that $u(\mathbf{x}, k) = e^{v(\mathbf{x}, k)}$. Substitution of $u(\mathbf{x}, k) = e^{v(\mathbf{x}, k)}$ in the Helmholtz equation (1) and a simple calculation give

$$\Delta v + \nabla v \cdot \nabla v = -k^2 \varepsilon_r(\mathbf{x}). \quad (7)$$

From now on, for the sake of presentation, we write $a \cdot a$ as a^2 for a complex-valued vector $a \in \mathbb{C}^3$. We eliminate $\varepsilon_r(\mathbf{x})$ from (7) by the differentiation of both sides of this equation with respect k , which is similar to the first step of the method of [6]. We obtain

$$\Delta \partial_k v + 2\nabla \partial_k v \cdot \nabla v = \frac{2\Delta v + 2(\nabla v)^2}{k}. \quad (8)$$

It is seen that if we can somehow find v from the latter equation then ε_r can be computed via (7). We observe in (8) that $\partial_k v$ and v are related as

$$v(\mathbf{x}, k) = - \int_k^{\bar{k}} \partial_k v(\mathbf{x}, s) ds + v(\mathbf{x}, \bar{k}).$$

Defining

$$q(\mathbf{x}, k) := \partial_k v(\mathbf{x}, k), \quad V(\mathbf{x}) := v(\mathbf{x}, \bar{k}), \quad (9)$$

and substituting in (8), we obtain a nonlinear integro-differential equation for q

$$\begin{aligned} & \frac{k}{2} \Delta q(\mathbf{x}, k) + k \nabla q(\mathbf{x}, k) \cdot \left(- \int_k^{\bar{k}} \nabla q(\mathbf{x}, s) s + \nabla V(\mathbf{x}) \right) \\ & = - \int_k^{\bar{k}} \Delta q(\mathbf{x}, s) s + \Delta V(\mathbf{x}) + \left(- \int_k^{\bar{k}} \nabla q(\mathbf{x}, s) s + \nabla V(\mathbf{x}) \right)^2. \end{aligned} \quad (10)$$

Now we complete the integro-differential equation formulation for our coefficient inverse problem by exploiting the data $g(\mathbf{x}, k) = u(\mathbf{x}, k)$ given on the boundary $\partial\Omega$. Recall that $u(\mathbf{x}, k) = e^{v(\mathbf{x}, k)}$, which deduces $\partial_k v(\mathbf{x}, k) = \partial_k u(\mathbf{x}, k)/u(\mathbf{x}, k)$. We hence have a Dirichlet boundary condition for $q(\mathbf{x}, k)$ on $\partial\Omega$ as

$$q(\mathbf{x}, k) = \psi(\mathbf{x}, k) \quad \text{on } \partial\Omega, \quad (11)$$

where

$$\psi(\mathbf{x}, k) := \frac{\partial_k g(\mathbf{x}, k)}{g(\mathbf{x}, k)} \quad \text{on } \partial\Omega.$$

We have obtained a nonlinear integro-differential equation (10) for the function $q(\mathbf{x}, k)$ with the Dirichlet boundary condition (11). We call $V(\mathbf{x})$ the tail function. Both functions q and V in (10) are unknown. To solve our inverse problem, both these functions need to be approximated. This is done by an iterative process, where we start the iterations from an initial approximation $V_0(\mathbf{x})$ for the tail function $V(\mathbf{x})$. We will describe later in section 3.4 how to find $V_0(\mathbf{x})$, which is a crucial step in our method. Given V_0 , we find $q(\mathbf{x}, k)$ by solving (10) and then compute $\varepsilon_r(\mathbf{x})$ using (7). This ends the first iteration. The next iterations follow a similar procedure but they use an updated tail function V instead of its initial approximation V_0 . Here we observe that we need ∇V and ΔV instead of V in our computation. The gradient of the updated tail is computed by $\nabla V(\mathbf{x}) = \nabla u(\mathbf{x}, \bar{k})/u(\mathbf{x}, \bar{k})$, where $u(\mathbf{x}, \bar{k})$ is obtained by solving the Lippman-Schwinger equation (6) in Ω with ε_r obtained from the previous iteration. Recall that $\Delta V = \text{div}(\nabla V)$. This is an analog of the well known predictor-corrector procedure, where updates for V are predictors and updates for q and ε_r are correctors.

3.2 Discretization with respect to the wavenumber

To find q and V from (10)–(11) using an iterative process, we consider a discretization of (10)–(11) with respect to the wavenumber k . We divide the interval $[\underline{k}, \bar{k}]$ into N subintervals with

the uniform step size $h = k_{n-1} - k_n$ as follows

$$\underline{k} = k_N < k_{N-1} < \dots < k_1 < k_0 = \bar{k}. \quad (12)$$

We approximate the function $q(\mathbf{x}, k)$ as a piecewise constant function with respect to $k \in [k, \bar{k}]$. More precisely, we assume that

$$q(\mathbf{x}, k) = q_n(\mathbf{x}), \quad \text{for } k \in [k_n, k_{n-1}). \quad (13)$$

For $k \in [k_n, k_{n-1})$, the latter approximation implies that

$$\int_k^{\bar{k}} q(\mathbf{x}, s) ds = (k_{n-1} - k)q_n(\mathbf{x}) + h \sum_{j=0}^{n-1} q_j(\mathbf{x}), \quad (14)$$

where $q_0(\mathbf{x}) = 0$. Using (13) and (14) we rewrite problem (10)–(11) for $k \in [k_n, k_{n-1})$ as

$$\begin{aligned} (k_{n-1} - k/2)\Delta q_n - F_n \cdot \nabla q_n - k_{n-1}(k_{n-1} - k)(\nabla q_n)^2 &= G_n \quad \text{in } \Omega \\ q_n &= \psi_n \quad \text{on } \partial\Omega, \end{aligned} \quad (15)$$

where

$$\begin{aligned} F_n &= (k + 2(k_{n-1} - k))(h \sum_{j=0}^{n-1} \nabla q_j + \nabla V_{n-1}), \\ G_n &= (h \sum_{j=0}^{n-1} \nabla q_j)^2 - h \sum_{j=0}^{n-1} \Delta q_j - 2h \nabla V_{n-1} \cdot \sum_{j=0}^{n-1} \nabla q_j + \Delta V_{n-1} + (\nabla V_{n-1})^2. \end{aligned}$$

We indicate here the dependence of the tail function $V := V_n$ on n since we approximate V iteratively as outlined in the end of section 3.1. Now assuming that the step size h is sufficiently small and that $h\bar{k} \ll 1$, we ignore those terms in (15), whose absolute values are $O(h)$ as $h \rightarrow 0$. We note that these small terms include the nonlinear term $k_{n-1}(k_{n-1} - k)(\nabla q_n)^2$ for q_n .

Even though the left hand side of equation (15) depends on k , it changes very little with respect to $k \in [k_n, k_{n-1})$ since the interval $[k_n, k_{n-1})$ is small. Hence, we eliminate this k -dependence by integrating both sides of (15) with respect to $k \in (k_n, k_{n-1})$ and then dividing both sides of the resulting equation by h . We obtain the Dirichlet boundary value problem

$$\Delta q_n - \tilde{F}_n \cdot \nabla q_n = \frac{\tilde{G}_n}{k_{n-1}} \quad \text{in } \Omega \quad (16)$$

$$q_n = \psi_n \quad \text{on } \partial\Omega, \quad (17)$$

where

$$\begin{aligned} \tilde{F}_n &= (k_n/k_{n-1} + 1)(h \sum_{j=0}^{n-1} \nabla q_j + \nabla V_{n-1}), \\ \tilde{G}_n &= -2h \sum_{j=0}^{n-1} \Delta q_j - 4h \nabla V_{n-1} \cdot \sum_{j=0}^{n-1} \nabla q_j + 2\Delta V_{n-1} + 2(\nabla V_{n-1})^2. \end{aligned}$$

We refer to the paper [19] for more details of the derivation of the Dirichlet boundary value problem (16)–(17) as well as its solvability. Now we are ready to summarize the globally convergent method as a computational algorithm in the next section.

3.3 The algorithm

In the algorithm below we use i for the inner iterations which play a role in updating the tails as indicated in [2, 19].

Algorithm 1 Globally convergent algorithm

- 1: Given ∇V_0 , set $q_0 := 0$
 - 2: **for** $n = 1, 2, \dots, N$ **do**
 - 3: Set $q_{n,0} := q_{n-1}$ and $\nabla V_{n,0} := \nabla V_{n-1}$
 - 4: **for** $i = 1, 2, \dots, I_N$ **do**
 - 5: Find $q_{n,i}$ by solving the boundary value problem (16)–(17)
 - 6: Update $\nabla v_{n,i} := -(h\nabla q_{n,i} + h \sum_{j=0}^{n-1} \nabla q_j) + \nabla V_{n,i-1}$ in Ω
 - 7: Update $\varepsilon_{rn,i}$ via (7)
 - 8: Find $u_{n,i}(\mathbf{x}, \bar{k})$ by solving LS equation (6) in Ω with $\varepsilon_r := \varepsilon_{rn,i}$
 - 9: Update $\nabla V_{n,i}(\mathbf{x}) := \nabla u_{n,i}(\mathbf{x}, \bar{k})/u_{n,i}(\mathbf{x}, \bar{k})$
 - 10: **end for**
 - 11: Update $q_n := q_{n,I_N}$, $\varepsilon_{rn} := \varepsilon_{rn,I_N}$ and $\nabla V_n := \nabla V_{n,I_N}$
 - 12: **end for**
 - 13: Choose ε_r by *the-criterion-of-choice*
-

Remark 2 (i) *The criterion for choosing the final result for ε_r and the stopping rules with respect to n and i in the iterations are addressed in section 5.3 of the numerical implementation. We also refer to [2, 18, 20, 28] for stopping criteria developed for the numerical verification for globally convergent methods. Recall that the number of iterations is often considered as a regularization parameter in the theory of ill-posed problems, see for instance [2].*

(ii) *We refer to section 5.1 for some details about the truncation and smoothing that is used when updating $\varepsilon_{rn,i}$ via (7).*

It can be seen from the algorithm that its main computational part of the algorithm is to solve at each iteration the Dirichlet boundary value problem (16)–(17) and the Lippmann-Schwinger equation (6). Recall that the well-posedness of these two problems have been established, see [19] for the boundary value problem and [11] for Lippmann-Schwinger equation. Some details about solving these two problems can be found in the section 5.1 of the numerical implementation.

3.4 The initial approximation $V_0(\mathbf{x})$ for the tail function

The initial approximation V_0 of the tail function plays an important role in both numerical implementation and the convergence analysis. We refer to [19] for more details on how

the convergence of the algorithm depends on the initial tail function. Using an asymptotic expansion with respect to k for the solution $u(\mathbf{x}, k)$ to the forward problem (1)–(3) it has been shown in [19] that there exists a function $p(\mathbf{x}) \in C^2(\bar{\Omega})$ such that

$$\log u(\mathbf{x}, k) = -ikp(\mathbf{x})(1 + O(1/k)), \quad \text{as } k \rightarrow \infty. \quad (18)$$

Since \bar{k} is sufficiently large, then dropping the term $O(1/k)$ in (18) for $k \geq \bar{k}$, we obtain $v(\mathbf{x}, k) = \log u(\mathbf{x}, k) = -ikp(\mathbf{x})$ for $k \geq \bar{k}$. Hence, we approximate the initial tail function as

$$V(\mathbf{x}) = -i\bar{k}p(\mathbf{x}). \quad (19)$$

Since by (9) $q(\mathbf{x}, k) = \partial_k v(\mathbf{x}, k)$, then $q(\mathbf{x}, \bar{k}) = -ip(\mathbf{x})$. Substituting these approximations in (10) and (11) at $k = \bar{k}$, we obtain that the function $p(\mathbf{x})$ is the solution of the following Dirichlet boundary value problem

$$\Delta p(\mathbf{x}) = 0 \quad \text{in } \Omega, \quad (20)$$

$$p(\mathbf{x}) = i\psi(\mathbf{x}, \bar{k}) \quad \text{on } \Gamma. \quad (21)$$

We refer to [19] for more details on the derivation of the latter boundary value problem as well as a discussion on its unique solvability.

Therefore, for the initial approximation V_0 of the tail function V we take

$$V_0(\mathbf{x}) = i\bar{k}p(\mathbf{x}) \quad (22)$$

where $p(\mathbf{x})$ is computed by solving problem (20)–(21). It has been proved in [19], using the Schauder theorem [21], that the accuracy of this initial approximation depends only on the error in the boundary data

$$\|V_0(\mathbf{x}) - V(\mathbf{x})\|_{C^{2,\alpha}(\bar{\Omega})} \leq C\bar{k}\|\psi(\mathbf{x}, \bar{k}) - \psi_{\text{exact}}(\mathbf{x}, \bar{k})\|_{C^{2,\alpha}(\partial\Omega)},$$

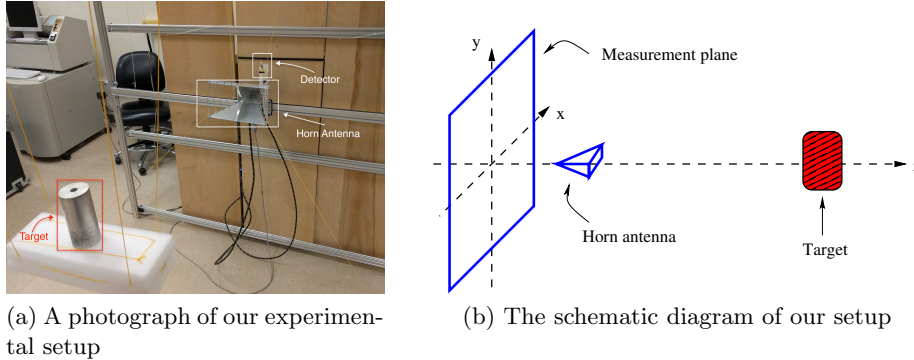
where $C = C(\Omega)$ is a positive constant depending only on the domain Ω and $C^{2,\alpha}(\Omega)$ is the Hölder space. This means that the error in the first tail function depends only on the error in the boundary data. Therefore, we obtain a good approximation for the tail function already in the zero iteration of our algorithm. However, our numerical experience tell us that we need to do more iterations. The approximation (19) and, as a result, the assumption (22) form our reasonable approximate mathematical assumption mentioned in Introduction. We note that (19) and (22) are used only on the zero iteration of our algorithm and are not used for other tail functions, which are obtained in the iterative process of our algorithm.

With the choice (22) of V_0 , it was proved in [19] that the algorithm proposed in section 3.3 converges in the sense that it provides a good approximation for the coefficient $\varepsilon_r(\mathbf{x})$. The accuracy of this approximation depends only on the noise in the backscatter data, discretization step size h and the domain Ω . We note that no a priori information about a small neighborhood of the unknown coefficient is used here. Therefore we say that our algorithm is globally convergent within the approximation framework (19).

4 Experimental data and preprocessing

We describe in this section the experimental setup, how the data were collected, and an important part of this paper: the data preprocessing procedure.

4.1 Data collection



(a) A photograph of our experimental setup

(b) The schematic diagram of our setup

Figure 1: The experimental setup.

The measurement data has been collected in a regular room, see Figure 1. As mentioned in Introduction, keeping in mind our desired applications, we did not want to arrange a special anechoic chamber. On the measurement plane, which is a 1 m by 1 m area, we define that the x -axis and the y -axis are the horizontal and the vertical axis, respectively, while the z -axis is perpendicular to the measurement plane. The direction from the target, whose front face is positioned at $z = 0$, to the measurement plane is the negative direction of the z -axis.

The source and receiver in the experiments are both from the same device, a 2 port Rohde & Schwarz vector network analyzer (VNA), connected by 2-meter Megaphase RF Killer Bee test cables. The broadband horn antenna and the collecting probe are both connected to the VNA. The antenna is positioned at a distance of about 75 cm from the targets and 18 cm from the “wooden wall” of Figure 1(a), where the probe (i.e. detector) is located. For some technical reasons it was impossible to place the antenna behind that “wooden wall”. The VNA sends single frequency signals at frequencies ranging from 1 GHz to 10 GHz via the horn antenna. Actually by design the signal is also emitted from the probe at the same time. This probe technically collects both emitted and reflected signals, more precisely their scattering parameters (S -parameters). However, the VNA is designed such that the reflection in the signal to each device is calibrated, that is, the internal reflections are removed. Therefore, the measured data are supposed to be as close to just the wave scattered by the unknown target as possible. For the range of frequencies from 1 GHz to 10 GHz we collect the scattered wave at 300 frequency points uniformly distributed over that range.

To obtain the backscatter data on the measurement plane for a single incident wave the experiment is repeated for different positions of the probe on the measurement plane, which is the above mentioned wooden wall. More precisely, the probe is uniformly moved over the

scanning area with the step size 2 cm, that means a total of 2550 data points. We scale to dimensionless variables by considering $\mathbf{x} = \mathbf{x}/(10 \text{ cm})$ for the convenience in our numerical implementation. Therefore, from now on when we see, for example 0.75 of length this means 7.5 cm. Let $\mathbf{E} = (E_x, E_y, E_z)$ be the electric field. The component E_y was incident upon the medium and the backscatter signal of the same component was measured. As it is stated in section 4.2.2, our central frequency is 3.1 GHz which corresponds to the wavelength $\lambda = 9.67 \text{ cm}$. This means that the source/target distance was 7.75λ . Since this distance is sufficiently large in terms of λ , we have treated the incident wave as a plane wave $E_{y,inc} = e^{ikz}$.

4.2 Data preprocessing

The mismatch between experimental data and simulated data is huge as one can see in Figure 2. Therefore, to invert the measured data using the globally convergent method, we need a *heuristic* data preprocessing procedure. The goal of the latter process, which mainly includes data propagation, truncation and calibration, is to make the experimental data somehow look similar to computationally simulated data.

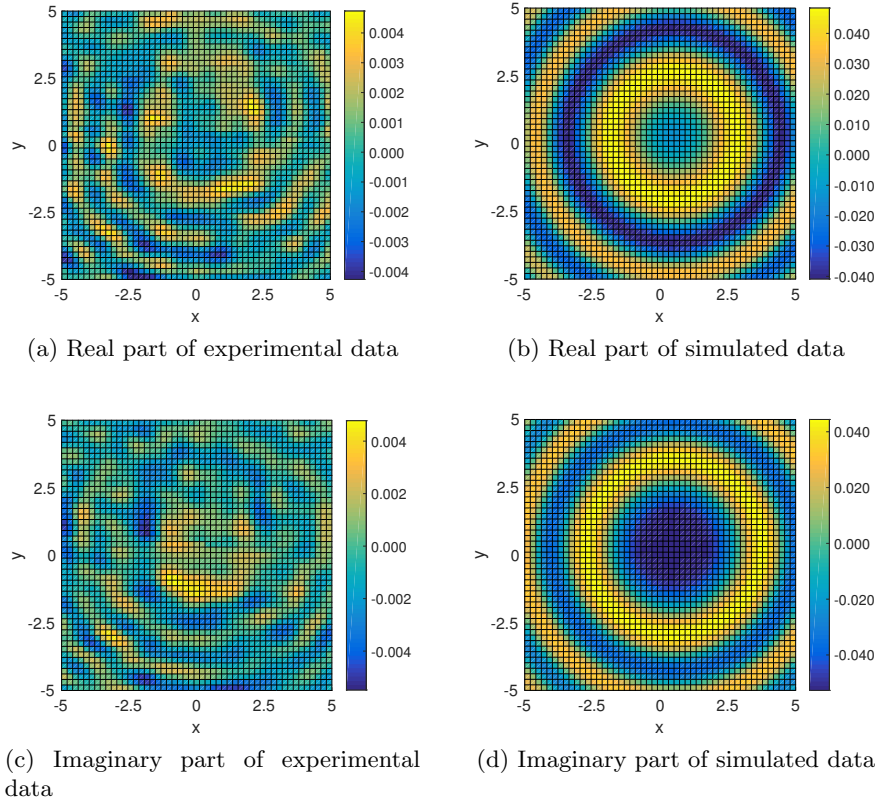


Figure 2: The experimental data (left) and the simulated data (right) on the measurement plane (xy -plane).

4.2.1 Data propagation

This is one of the most important steps in data preprocessing. Given the experimental data on the measurement plane, the data propagation process aims to approximate these data on a plane which is closer to the unknown target than the measurement plane. This process firstly reduces the computational domain for our algorithm and secondly makes the scattered field data to look more focused. This is done using a well known method in optics called the angular spectrum representation, see, e.g., [23, Chapter 2]. We note that this technique has been successfully exploited in [28] for data preprocessing for the globally convergent method of [2].

We recall that the negative z -direction is from the target to the measurement plane. Denote by $g(\mathbf{x}, k)$ the experimental data defined on the measurement rectangle $P_m = \{\mathbf{x} : -5 < x < 5, -5 < y < 5, z = b\}$ of the plane $\{z = b\}$ and by $f(\mathbf{x}, k)$ its approximation on the propagated rectangle $P_p = \{\mathbf{x} : -5 < x < 5, -5 < y < 5, z = a\}$ of the plane $\{z = a\}$. We set both functions g and f to be equal to zero on those parts of corresponding planes $\{z = b\}$ and $\{z = a\}$ which are outside of those rectangles. Abusing notations a little bit, we call below sets P_m and P_p “measurement plane” and “propagated plane” respectively. We have $b < a < 0$ since P_p is closer to the target than P_m . Using the method of the angular spectrum representation, we obtain

$$f(x, y, a, k) = \iint_{k_x^2 + k_y^2 < k^2} \hat{g}(k_x, k_y, k) e^{i[k_x x + k_y y - k_z(a-b)]} k_x k_y,$$

where

$$\hat{g}(k_x, k_y, k) = \iint_{\mathbb{R}^2} g(x, y, b, k) e^{-i(k_x x + k_y y)} \underline{x} \underline{y}, \quad k_z = (k^2 - k_x^2 - k_y^2)^{1/2}. \quad (23)$$

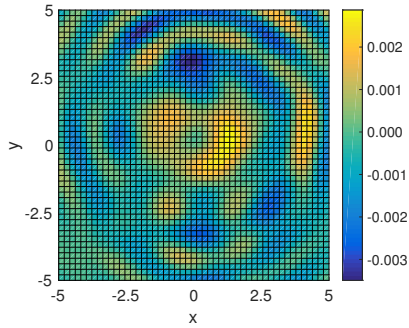
The idea of the method is that we consider the Helmholtz equation satisfied by the total wave outside the scattering medium ($\varepsilon_r(\mathbf{x}) = 1$). Then the Fourier transform with respect to x and y of the total field satisfies an ordinary differential equation in the z -direction. Together with the radiation condition and the boundary condition on the measurement plane P_m one can solve the 1D problem and obtain the formula (23). We refer to [23, 28] for more details on the angular spectrum representation. In Figure 3(d) we present the absolute value of the experimental data on the propagated plane

$$P_p = \{\mathbf{x} : -5 < x < 5, -5 < y < 5, z = -0.75\}, \quad (24)$$

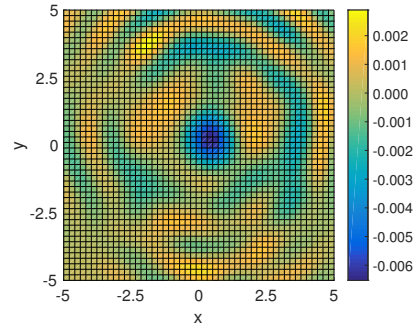
computed by the formula (23) for the wavenumber $k = 6.575$. Comparing Figure 3(c) and Figure 3(d), we can easily see that the focusing of the scattered field is considerably improved after data propagation.

4.2.2 Choosing a stable frequency interval

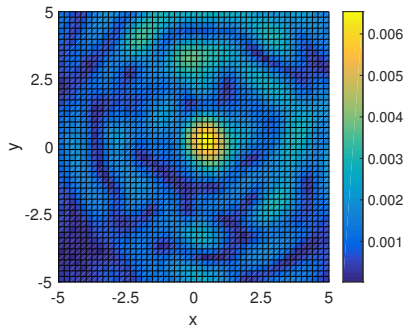
We recall that for each of 300 frequencies from 1 GHz to 10 GHz the measured data is a set of 2550 points uniformly distributed on the measurement plane. An important fact to note is that the data both before and after propagation are stable only for a certain small



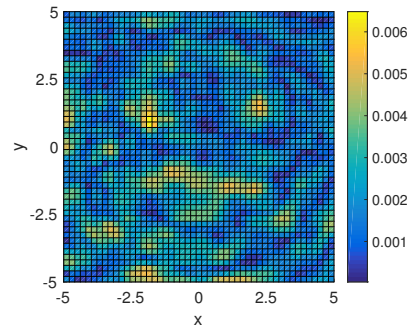
(a) Real part of propagated data



(b) Imaginary part of propagated data



(c) Absolute value of propagated data



(d) Absolute value of measured data

Figure 3: We respectively display in (a), (b) and (c) the real, imaginary and absolute value of the propagated data. The absolute value of the measured data before propagation is in (d) (its real and imaginary part are presented in Figure 2).

interval of frequencies. By stable here we mean that the variation of the data with respect to the frequency is relatively small. Therefore, choosing an interval of frequencies for which the data is most stable or equivalently its variation with respect to the frequency in that interval is the smallest compared to any other intervals is essential for our algorithm.

We choose such an interval by manually plotting the absolute value of the propagated data for all frequencies. It turned out that the data is most focused and stable with respect to the frequency around 3.1 GHz; this can also be seen in Figure 4, where we plot the absolute value of the propagated data, which is written as a matrix of 300×2550 . The stable interval of frequencies from Figure 4 is $[2.98, 3.19]$ GHz, that equivalently means, $[\underline{k}, \bar{k}] = [6.25, 6.70]$ is the stable interval of wavenumbers used in our theoretical setting in the previous sections. We have observed that the lower and upper bounds of such intervals differ only very slightly for the data of different targets considered in this paper. Note that we now consider only the propagated data since we will use these data instead of the original one.

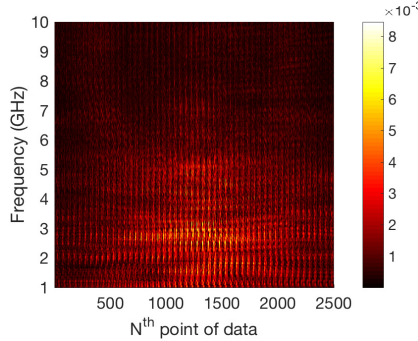


Figure 4: The absolute value of the experimental data after propagation for all frequencies ranging from 1 GHz to 10 GHz.

4.2.3 Truncation and calibration of propagated data

We know from section 4.2.2 that the variation with respect to the frequency of the propagated data around 3.1 GHz is the smallest compared to that of any other interval of frequencies. However, this variation is still not small enough for our algorithm. Furthermore, the behavior of the absolute value of the propagated data is still not close to those in simulations. Indeed, we observe that after data propagation the magnitude of the simulated data has a clear peak at the xy -location of the target for all frequencies, see Figure 5(b). For propagated measured data, although its magnitude always attains the maximum at the xy -location of the target for all frequencies around 3.1 GHz, it does not really have a clear peak as in simulations due to local maxima at other regions of the propagated plane, see Figure 3(c). However, those latter local maxima are not located at the same locations for different frequencies. On the other hand the global maximum is located at the same place for all frequencies around 3.1 GHz. From this important observation we guess that the target should be actually located in some small neighborhood of the global maximum of the propagated data.

To make the propagated measured data look more similar to those in simulations we truncate those by taking the points for which its magnitude is greater than or equal to 80% of its maximum value, and setting the rest to be zero. In other words, for each $k \in [\underline{k}, \bar{k}]$ we replace the function $f(x, y, a, k)$ with the function $\tilde{f}(x, y, a, k)$ where

$$\tilde{f}(x, y, a, k) = \begin{cases} f(x, y, a, k) & \text{if } |f(x, y, a, k)| \geq 0.8 \max_{x,y} |f(x, y, a, k)|, \\ 0 & \text{otherwise.} \end{cases} \quad (25)$$

After that we smooth the function $\tilde{f}(x, y, a, k)$ by a Gaussian filter, more precisely, we use the smoothing function `smooth3` in Matlab with the Gaussian option. This is done for all values of $k \in [\underline{k}, \bar{k}]$. We display in Figure 5 the propagated data after this procedure. It can be seen that the behavior of the absolute value of these processed data looks more similar to that of simulated data.

We are now at the last step of data preprocessing called data calibration. This process is to scale the amplitude of the measured data to the same scaling as in our simulations, since the experimental data and simulated data usually have quite different amplitudes. For example, in Figure 5, we can see that the maximal value of the absolute value of measured data is about 0.0065 while this value is about 0.4 for the simulated data. To do the scaling we need the so-called the calibration factor. For estimating the calibration factor, we use the measured data of a single calibrating object whose location, shape, size, and dielectric constant are known. The word ‘‘single’’ is important here to ensure that the calibration procedure is unbiased, that means, we are supposed to know such information for only the calibrating object.

For $k \in [\underline{k}, \bar{k}]$, where \underline{k} and \bar{k} are chosen from the process of choosing a stable frequency interval of section 4.2.2, let $U_{cal.obj}^{sim}(\mathbf{x}, k)$ and $U_{cal.obj}^{exp}(\mathbf{x}, k)$ be the propagated data of the simulated and measured scattered field for the calibrating object, respectively. We define our calibration factor as

$$A(k) = \frac{\max |U_{cal.obj}^{sim}(\mathbf{x}, k)|}{\max |U_{cal.obj}^{exp}(\mathbf{x}, k)|}.$$

It can be seen that the amplitude of $A(k)U_{cal.obj}^{exp}(\mathbf{x}, k)$ has the same scale to that of the simulated data. We use the calibration factor $A(k)$ for measured data of all other objects. More precisely, given the propagated and truncated scattered field data $\tilde{f}(x, y, a, k)$ in (25), we consider $A(k)\tilde{f}(x, y, a, k) + e^{ikz}$ as the input for our algorithm in section 3.3. We emphasize that this calibration factor is computed using the geometrical and physical information of only a single object: the calibrating object.

5 Numerical implementation and reconstruction results

We describe in this section some details of the numerical implementation and present the reconstruction results for our experimental data using the globally convergent algorithm. Due to some technical limitations, we have collected experimental data for five objects. So, we test here these five data sets. Each data set corresponds to a single scattering object,

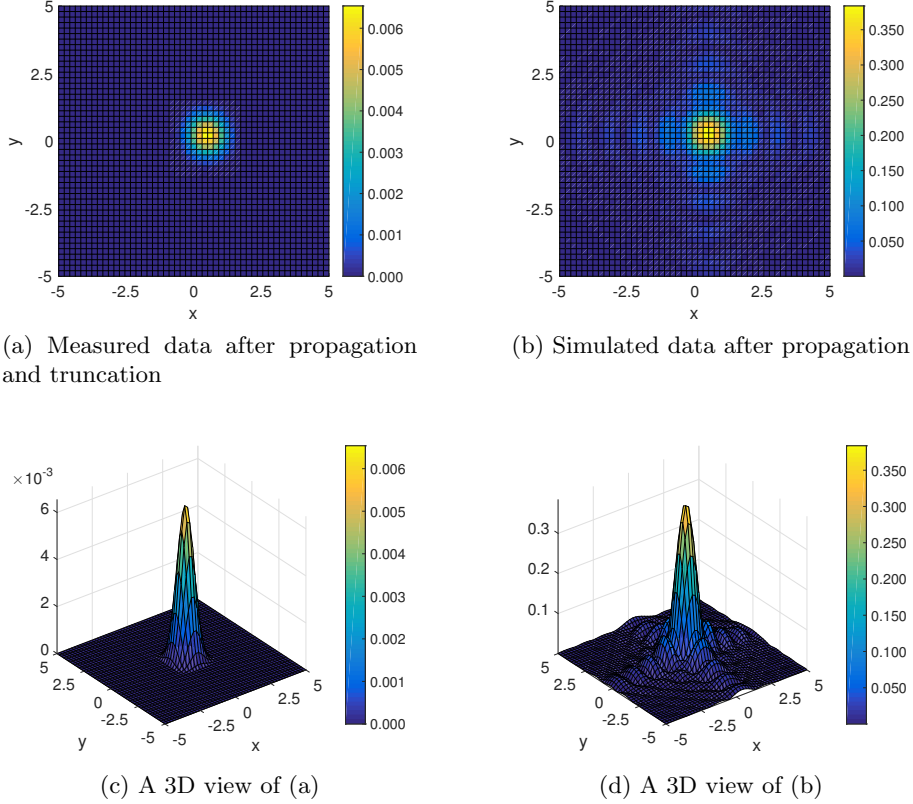


Figure 5: We display on the propagated plane the absolute value of the simulated data and the experimental data in which the latter has been truncated as described in section 4.2.3.

numbered from 1 to 5, see Table 1. Object 1 (a piece of yellow pine) is chosen as our calibrating object.

5.1 Some computational details

In our numerical implementation the front face of the target is positioned at $\{z = 0\}$. We consider the computational domain Ω as

$$\Omega = (-2.5, 2.5) \times (-2.5, 2.5) \times (-0.75, 4.25).$$

Here we propagate all the measured data to the rectangle P_p located on the plane $\{z = -0.75\}$ and search for the unknown targets in the range $(-0.75, 1)$ of the z -direction. This search range is motivated by both: similar ranges that have been used in [27, 28] and our desired applications for detection of hidden explosives. Indeed, $z \in (-0.75, 1)$ means that the linear size of the target in the z -direction does not exceed 17.5 cm. It is well-known that typical linear size of antipersonnel mines and IEDs are between 5 cm and 15 cm. We note that the

Table 1: Scattering objects

Object ID	Name of the object
1	A piece of a yellow pine
2	A piece of a wet wood
3	A geode
4	A tennis ball
5	A baseball

larger range $(-0.75, 4.25)$ is considered for the goal of completing the backscatter data in the next section. Also in the xy -plane we restrict ourselves to the smaller area $(-2.5, 2.5)^2$ than the original measurement one $(-5, 5)^2$. The main reason comes from the observation that the truncated data is zero outside the area $(-2.5, 2.5)^2$, see Figure 5, and does not contribute to the reconstruction process. This restriction helps us reduce our computational domain.

To solve the Lippmann-Schwinger integral equation (6), we use a spectral method developed by G. Vainikko in [29]. This method exploits a periodization technique of the integral equation introduced by that author, which enables the use of the fast Fourier transform and a simple numerical implementation. We use the method of Vainikko to find the solution in a box containing the support of the function $\varepsilon_r - 1$. The solution in the complement of the box in Ω is then computed by the integration in (6). We solve the boundary value problem (16)–(17) by a finite element method. More precisely, we use FreeFem++ [16], a standard software designed with a focus on solving partial differential equations using finite element methods. We refer to www.freefem.org for more information about FreeFem++.

We observe from data preprocessing that the location of a target in the xy -plane can be roughly estimated from the propagated data. Indeed, we define Ω_T as

$$\Omega_T = \{(x, y) : |f_{prop}^{trun}(\mathbf{x}, k)| > 0.7 \max |f_{prop}^{trun}(\mathbf{x}, k)|\} \subset P_p,$$

where $f_{prop}^{trun}(\mathbf{x}, k)$ is the measured data on the propagated plane $\{z = -0.75\}$ after the above truncation. Note that for each target the absolute value of $f_{prop}^{trun}(\mathbf{x}, k)$ has a positive peak whose location is the same for all $k \in [\underline{k}, \bar{k}]$, see Figure 5. The truncation value 0.7 was chosen based on trial-and-error tests on simulated and calibrating targets. We observed that Ω_T provides a reasonable approximation for the xy -location of a target. The same truncation was applied to all targets. Hence, it is not biased. Using Ω_T and the assumption that we seek for the target in $(-0.75, 1)$ of the z -direction, the coefficient $\varepsilon_{rn,i}$ is truncated as follows

$$\varepsilon_{rn,i}(\mathbf{x}) := \begin{cases} \max(|\varepsilon_{rn,i}(\mathbf{x})|, 1), & \mathbf{x} \in \Omega_T \times (-0.75, 1), \\ 1, & \text{elsewhere.} \end{cases}$$

After that it is smoothed by `smooth3` in Matlab with the Gaussian option as in data truncation. The so obtained $\varepsilon_{rn,i}$ is then used for solving the Lippmann-Schwinger equation in Algorithm 1.

Another important detail we would like to mention is a modification for approximating the data $\psi(\mathbf{x}, k) = \partial_k g(\mathbf{x}, k)/g(\mathbf{x}, k)$ on $\Gamma = \{\mathbf{x} \in \partial\Omega : z = -0.75\}$, where $g(\mathbf{x}, k) =$

$A(k)f_{prop}^{trun}(\mathbf{x}, k) + e^{ikz}$. The function $g(\mathbf{x}, k)$ is supposed to be as close to the total field as possible and $\psi(\mathbf{x}, k)$ should be smooth with respect to k . However, the variation of $\psi(\mathbf{x}, k)$ with respect to k in the small interval $[\underline{k}, \bar{k}]$ is actually not small, since the behavior of $g(\mathbf{x}, k)$ with respect to k is not similar to that of the corresponding total field in simulations. The latter is one of discrepancies between simulated and propagated experimental data. We observe from simulations that on the propagated plane the absolute value of the total field in our stable range of frequencies typically has a global minimum at the xy -location of the scatterer. Note that the maximum we see in Figure 5 is for the uncalibrated scattered field. Motivated by this observation, we approximate $\psi(\mathbf{x}, k) = \partial_k g(\mathbf{x}, k)/g(\mathbf{x}, k)$ by $\tilde{\psi}(\mathbf{x}, k) = \partial_k g(\mathbf{x}, k)/g(\mathbf{x}, k^*)$, where we choose such a value k^* for which $|g(\mathbf{x}, k)|$ has a global minimum. By doing so, we see that the variation of $\tilde{\psi}(\mathbf{x}, k)$ in k becomes small enough, when compared with those in simulations to be used in the algorithm.

5.2 Completing the backscatter data

We recall that only the backscatter signals were measured in our experiments. This means that after the above data preprocessing procedure, the function $g(\mathbf{x}, k)$ was known only on the side $\Gamma = \{\mathbf{x} \in \partial\Omega : z = -0.75\}$ of the domain Ω . As in [19, 27], we replace the missing data on the other parts of Ω by the corresponding solution of the forward problem in the homogeneous medium, where $\varepsilon_r(\mathbf{x}) = 1$. In other words, in our computation, the function $g(\mathbf{x}, k)$ is extended on the entire boundary $\partial\Omega$ as

$$g(\mathbf{x}, k) := \begin{cases} g(\mathbf{x}, k), & \mathbf{x} \in \Gamma, \\ e^{ikz}, & \mathbf{x} \in \partial\Omega \setminus \Gamma. \end{cases} \quad (26)$$

We remark that data completion methods are widely used for inverse problems with incomplete data. The data completion (26) is a heuristic technique relying on the successful experiences of our group when working with globally convergent methods for experimental data, see [3, 27]. Other data completion methods may also be applied.

5.3 The stopping criteria and choosing the final result

Now we introduce the rules for stopping the iterations and choosing the final result for our Algorithm 1 relying on the content of the convergence theorem [19] and trial-and-error testing for simulated data. Indeed, the global convergence theorem 7.1 of [19] only claims that functions $\varepsilon_{rn,i}$ are located in a sufficiently small neighborhood of the true solution if the number of iterations is not too large. But this theorem does not claim that these functions tend to the exact solution, also see theorem 2.9.4 in [2] and theorem 5.1 in [3]. This implies that the stopping criteria should be chosen computationally.

We have two stopping criteria: one for the inner iterations and the second one for the outer iterations. Before stating those criteria precisely we need some definitions. Denote by $e_{n,i}$ the relative error between the two computed coefficients corresponding to two consecutive

inner iterations of the n -th outer iteration

$$e_{n,i} = \frac{\|\varepsilon_{rn,i} - \varepsilon_{rn,i-1}\|_{L^2(\Omega)}}{\|\varepsilon_{rn,i-1}\|_{L^2(\Omega)}}, \quad i = 2, 3, \dots \quad (27)$$

Consider the n -th and $(n + 1)$ -th outer iterations which contains I_1 and I_2 inner iterations, respectively. We define the sequence of relative errors associated to these two outer iterations as

$$e_{n,2}, \dots, e_{n,I_1}, \tilde{e}_{n+1,1}, e_{n+1,2}, \dots, e_{n+1,I_2}, \quad (28)$$

where

$$\tilde{e}_{n+1,1} = \frac{\|\varepsilon_{rn+1,1} - \varepsilon_{rn,I_1}\|_{L^2(\Omega)}}{\|\varepsilon_{rn,I_1}\|_{L^2(\Omega)}}.$$

The inner iterations with respect to i of the n -th outer iteration in the algorithm 1 are stopped when either $e_{n,2} < 10^{-6}$ or $i = 3$. Note that this rule is similar to the one used for “Test 2” in [27], where the maximal number of inner iterations is set up to be 5. During our numerical experiments we observed that the reconstruction results are essentially the same when we use either 3 or 5 for the maximal number of inner iterations.

Concerning the outer iterations with respect to n in Algorithm 1, it can be seen from the stopping rule for the inner iterations that each outer iteration consists of at least 2 and at most 3 inner iterations. Equivalently, the error sequence (28) has at least 3 and at most 5 elements. We stop the outer iterations if there are two consecutive outer iterations for which their error sequence (28) has three consecutive elements less than or equal to 5×10^{-4} . We emphasize again that we have no mathematical justification for these stopping rules; they rely on the content of the convergence theorem [19] and trial-and-error testing for simulated data.

We choose the final result for $\varepsilon_r(x)$ by taking the average of its approximations $\varepsilon_{rn,i}(x)$ corresponding to the relative errors in (28) that meet the stopping criterion for outer iterations. The computed dielectric constant is determined as the maximal value of the computed $\varepsilon_r(\mathbf{x})$. We have observed in our numerical studies that we need no more than five outer iterations to obtain the final result.

5.4 Summary of reconstruction results

We present in Table 2 the reconstruction results for the dielectric constant of the scattering objects under consideration. The second column of the table is the dielectric constant at 3 GHz of the scattering objects, independently measured by physicists from the Department of Physics and Optical Science at the University of North Carolina Charlotte (M. A. Fiddy and S. Kitchin). The percent number in the brackets is the error in the measurement given by the standard deviation. The measured relative permittivity of object 5 (a baseball) was not available due to some technical issues.

Our reconstruction results and their relative errors compared with measured dielectric constants are in the last two columns of the table. The error shows a very good accuracy for our reconstructions: only a few percent. The dielectric constant of object 2 (wet wood) is

relatively high which leads to the worst error case in computations, as anticipated. We have obtained best errors in objects 1 and 3. Note that object 1 is the calibrating object. We also observe that the computational error in object 4 is 2.5 times less than its measurement error.

Table 2: Measured and computed dielectric constant of the targets

Obj. ID	Measured ε_r (std. dev.)	Computed ε_r	Relative error
1	5.30 (1.6%)	5.44	2.6%
2	8.48 (4.9%)	7.60	10.3%
3	5.44 (1.1%)	5.55	2.0%
4	3.80 (13.0%)	4.00	5.2%
5	not available	4.76	n/a

We display in Figures 6, 7 and 8 the 3D-visualizations of exact and reconstructed geometry of the first four targets using `isosurface` in Matlab. In the isosurface plotting the isovalue was chosen to be 50% of the maximal value of the computed ε_r . This choice is simply based on the calibrating object and is applied to all other objects. From the figures we can see that locations of the targets are well-reconstructed. It can also be seen that although the shape reconstruction of targets is in general not very good, the results for spherical shaped objects 3, 4 and 5 seem to be better than those of rectangular prism ones (objects 1 and 2), which is reasonable.

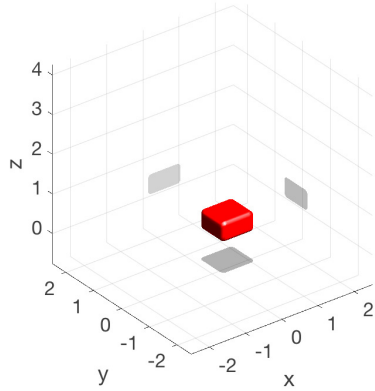
In conclusion, we can see from the reconstruction results that, under the above procedure of data preprocessing, our multi-frequency globally convergent method can image quite well the dielectric constants and locations of targets for our experimental data. This is achieved regardless on the fact that there is a huge misfit between these data and simulations. We note that these are only backscatter data associated with a single incident field. Moreover, the method can reconstruct relatively large inclusion/background contrasts, the case that is well known to be difficult for conventional least-squares approaches.

Acknowledgements

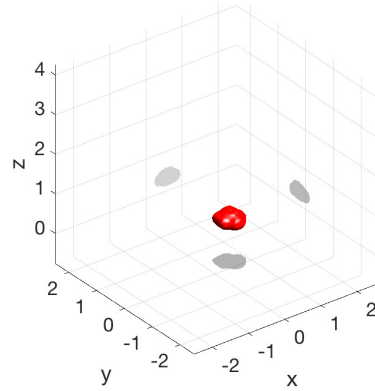
The authors are grateful to Mr. Steven Kitchin for his excellent work on data collection. This work was supported by US Army Research Laboratory and US Army Research Office grant W911NF-15-1-0233 and by the Office of Naval Research grant N00014-15-1-2330.

References

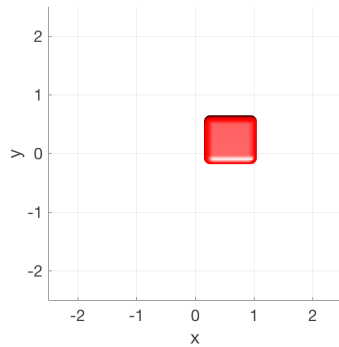
- [1] A. B. BAKUSHINSKY AND M. Y. KOKURIN, *Iterative Methods for Approximate Solutions of Inverse Problems*, Springer Verlag, 2004.
- [2] L. BEILINA AND M. V. KLIBANOV, *Approximate Global Convergence and Adaptivity for Coefficient Inverse Problems*, Springer, New York, 2012.



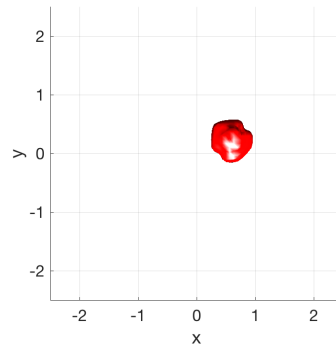
(a) Exact location and shape of object 1



(b) Reconstruction result of object 1



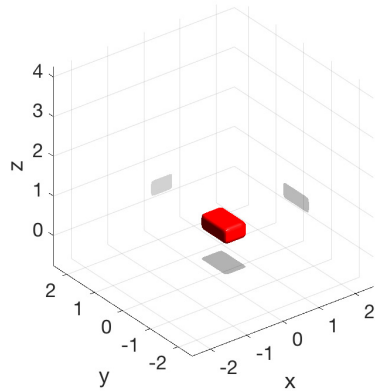
(c) A top view of (a)



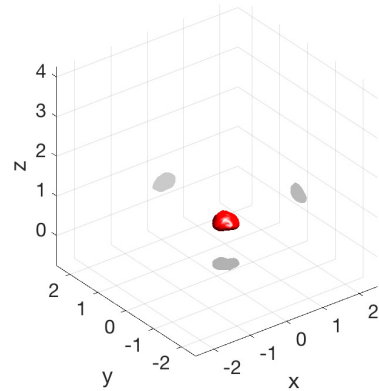
(d) A top view of (b)

Figure 6: Visualizations of exact (left) and reconstructed (right) location and shape of the scattering object 1. The top is a 3D view and the bottom is the top view.

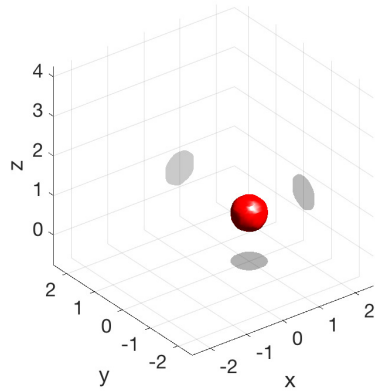
- [3] —, *A new approximate mathematical model for global convergence for a coefficient inverse problem with backscattering data*, *J. Inverse Ill-Posed Probl.*, 20 (2012), pp. 513–565.
- [4] K. BELKEBIR AND M. SAILLARD, *Special section on testing inversion algorithms against experimental data: inhomogeneous targets*, *Inverse Problems*, 21 (2005).
- [5] M. BORN AND E. WOLF, *Principles of Optics: Electromagnetic Theory of Propagation, Interference and Diffraction of Light*, Cambridge University Press, 7th ed., 1999.
- [6] A. L. BUKHGEIM AND M. V. KLIBANOV, *Global uniqueness of a class of multidimensional inverse problems*, *Soviet Math. Dokl.*, 24 (1981), pp. 244–247.



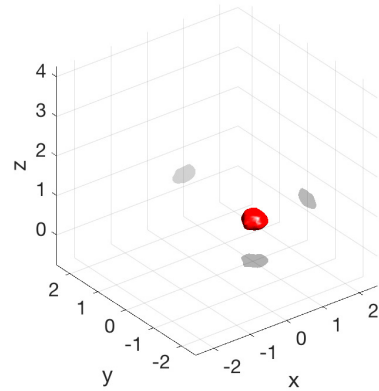
(a) Exact location and shape of object 2



(b) Reconstruction result of object 2



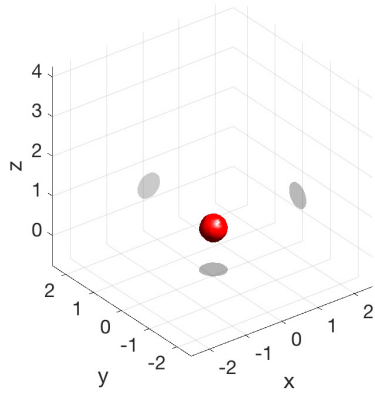
(c) Exact location and shape of object 3



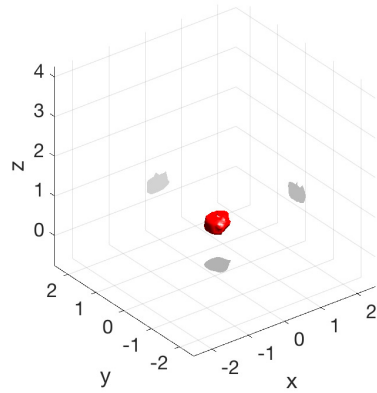
(d) Reconstruction result of object 3

Figure 7: 3D visualizations of scattering objects 2 and 3. The pictures in the left show exact location and shape of the targets while their reconstruction results are in the right.

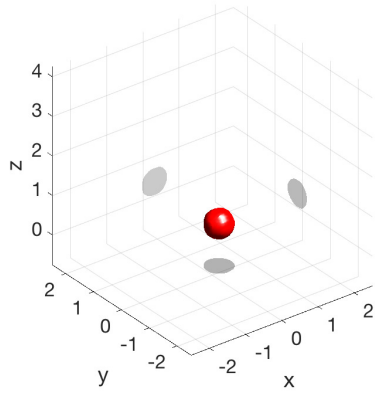
- [7] M. BURGER, B. KALTENBACHER, AND A. NEUBAUER, *Iterative solution methods*, in Handbook of Mathematical Methods in Imaging, O. Scherzer, ed., Springer, 2015, pp. 431–470.
- [8] M. BURGER AND S. OSHER, *A survey on level set methods for inverse problems and optimal design*, European J. of Appl. Math., 16 (2005), pp. 263–301.
- [9] G. CHAVENT, *Nonlinear Least Squares for Inverse Problems: theoretical foundations and step-by-step guide for applications*, Springer Netherlands, 2010.
- [10] L. F. CHEN, C. K. ONG, C. P. NEO, V. V. VARADAN, AND V. K. VARADAN, *Microwave Electronics: Measurement and Materials Characterization*, John Wiley &



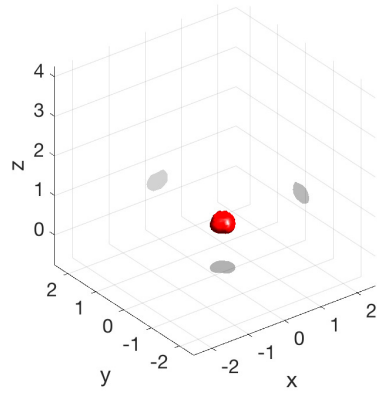
(a) Exact location and shape of object 4



(b) Reconstruction result of object 4



(c) Exact location and shape of object 5



(d) Reconstruction result of object 5

Figure 8: 3D visualizations of scattering objects 4 and 5. The pictures in the left show exact location and shape of the targets while their reconstruction results are in the right.

Sons Ltd, UK, 2004.

- [11] D. L. COLTON AND R. KRESS, *Inverse acoustic and electromagnetic scattering theory*, Springer, 2nd ed., 1998.
- [12] H. W. ENGL, M. HANKE, AND A. NEUBAUER, *Regularization of inverse problems*, Kluwer Acad. Publ., Dordrecht, Netherlands, 1996.
- [13] M. A. FIDDY AND R. S. RITTER, *Introduction to Imaging from Scattered Fields*, CRC Press; 1 edition, 2014.

- [14] J.-M. GEFFRIN, P. SABOUROUX, AND C. EYR, *Free space experimental scattering database continuation: experimental set-up and measurement precision*, Inverse Problems, 21 (2005), pp. S117–S130.
- [15] A. V. GONCHARSKY AND S. Y. ROMANOV, *Supercomputer technologies in inverse problems of ultrasound tomography*, Inverse Problems, 29 (2013), p. 075004 (22pp).
- [16] F. HECHT, *New development in FreeFem++*, J. Numer. Math., 20 (2012), pp. 251–265.
- [17] M. V. KLIBANOV, *Inverse problems and carleman estimates*, Inverse Problems, 8 (1992), pp. 575–596.
- [18] M. V. KLIBANOV, M. A. FIDDY, L. BEILINA, N. PANTONG, AND J. SCHENK, *Pico-second scale experimental verification of a globally convergent numerical method for a coefficient inverse problem*, Inverse Problems, 26 (2010), p. 045003.
- [19] M. V. KLIBANOV, H. LIU, AND L. H. NGUYEN, *A globally convergent method for a 3-D inverse medium problem for the generalized Helmholtz equation*, arxiv: 1605.06147, (2016).
- [20] A. V. KUZHUGET, L. BEILINA, M. V. KLIBANOV, A. SULLIVAN, L. NGUYEN, AND M. A. FIDDY, *Blind backscattering experimental data collected in the field and an approximately globally convergent inverse algorithm*, Inverse Problems, 28 (2012), p. 095007.
- [21] O. A. LADYZHENSKAYA AND N. N. URAL’TSEVA, *Linear and Quasilinear Elliptic Equations*, Academic Press, New York, London, 1969.
- [22] A. LITMAN AND L. CROCCO, *Special section on testing inversion algorithms against experimental data: 3D targets*, Inverse Problems, 25 (2009), p. 020201.
- [23] L. NOVOTNY AND B. HECHT, *Principles of Nano-Optics*, Cambridge University Press, Cambridge, UK, 2nd ed., 2012.
- [24] M. PASTORINO, *Microwave Imaging*, John Wiley & Sons, Hoboken, NJ, 2010.
- [25] R. POTTHAST, *A survey on sampling and probe methods for inverse problems*, Inverse Problems, 22 (2006), pp. R1–R47.
- [26] H. SCHUBERT AND A. KUZNETSOV, eds., *Detection and Disposal of Improvised Explosives*, Springer, Dordrecht, 2006.
- [27] N. T. THANH, L. BEILINA, M. V. KLIBANOV, AND M. A. FIDDY, *Reconstruction of the refractive index from experimental backscattering data using a globally convergent method*, SIAM J. Sci. Comput., 36 (2014), pp. 273–293.
- [28] ———, *Imaging of buried objects from experimental backscattering time dependent measurements using a globally convergent inverse algorithm*, SIAM J. Imaging Sci., 8 (2015), pp. 757–786.

- [29] G. VAINIKKO, *Fast solvers of the Lippmann-Schwinger equation*, in Direct and Inverse Problems of Mathematical Physics, D. Newark, ed., Int. Soc. Anal. Appl. Comput. 5, Dordrecht, 2000, Kluwer, p. 423.
- [30] J. C. WEATHERALL, J. BARBER, AND B. T. SMITH, *Identifying explosives by dielectric properties obtained through wide-band millimeter-wave illumination*, in Passive and Active Millimeter-Wave Imaging XVIII, D. Wikner and A. R. Luukanen, eds., vol. 9462, Proc. of SPIE, 2015, p. 94620F.
- [31] M. YAMAMOTO, *Carleman estimates for parabolic equations and applications*, Inverse Problems, 25 (2009), p. 123013.